

The molecular emission of the irradiated star forming core ahead of HH 80N

Josep M. Masqué¹, Josep M. Girart², Maria T. Beltrán¹, Robert Estalella¹

and

Serena Viti³

ABSTRACT

We present a Berkeley-Illinois-Maryland Association (BIMA) Array molecular survey of the star forming core ahead of HH 80N, the optically obscured northern counterpart of the Herbig-Haro objects HH 80/81. Continuum emission at 1.4 mm and 8 μm is detected at the center of the core, which confirms the presence of an embedded very young stellar object in the core. All detected molecular species arise in a ring-like structure, which is most clearly traced by CS (2–1) emission. This molecular ring suggests that strong molecular depletion occurs in the inner part of the core (at a radius of $\simeq 0.1$ pc and densities higher than $\sim 5 \times 10^4 \text{ cm}^{-3}$). Despite of the overall morphology and kinematic similarity between the different species, there is significant molecular differentiation along the ring-like structure. The analysis of the chemistry along the core shows that part of this differentiation may be caused by the UV irradiation of the nearby HH 80N object, that illuminates the part of the core facing HH 80N, which results in an abundance enhancement of some of the detected species.

Subject headings: ISM: individual (HH 80N) — ISM: molecules — radio lines: ISM — stars: formation — ISM: abundances —

1. Introduction

IRAS 18162–2048 is a high mass protostar, with a luminosity of $\sim 2 \times 10^4 L_{\odot}$, powering the most luminous and largest Herbig-Haro (HH) system, HH 80/81/80N, associated with a

¹Departament d’Astronomia i Meteorologia, Universitat de Barcelona, Martí i Franquès 1, 08028 Barcelona, Catalunya, Spain

²Institut de Ciències de l’Espai, (CSIC-IEEC), Campus UAB, Facultat de Ciències, Torre C5 - parell 2, 08193 Bellaterra, Catalunya, Spain

³Department of Physics and Astronomy, University College London, London, WC1E 6BT, UK

very highly collimated radio jet (Rodríguez et al. 1980; Reipurth & Graham 1988; Martí et al. 1993). This source is located in the GGD 27 region, at a distance of 1.7 kpc in Sagittarius (Rodríguez et al. 1980). A far-IR spectroscopic study of the HH 80/81/80N system shows that the FUV field radiated by the ionized material in the shock recombination region is able to induce the formation of a photodissociation region (PDR) in the surrounding medium of the HH objects and the jet flow (Molinari et al. 2001). The HH 80N object has not been detected in the optical neither at near infrared wavelengths, which is likely a consequence of the extinction due to a molecular cloud in the foreground (Martí et al. 1993).

A dense clump of $20 M_{\odot}$ was found ahead of HH 80N, firstly detected in ammonia (Girart et al. 1994) and afterward detected in other species, such as CS and HCO^+ (Girart et al. 1998). BIMA array observations (with $10''$ of angular resolution) carried out by Girart et al. (2001) (hereafter GEVWH) showed that the CS (2–1) emission traces a ring-like structure, with a radius of 0.24 pc, seen edge on. This observed morphology is most likely the result of a strong CS depletion in the inner region of the core (GEVWH). The analysis of the CS kinematics suggests that this structure is contracting with an infall velocity of 0.6 km s^{-1} . Assuming a gas temperature of 17 K, equivalent to the ammonia rotational temperature (Girart et al. 1994) the sound speed is $\sim 0.3 \text{ km s}^{-1}$, implying supersonic collapse. In addition, the CO (1–0) emission reveals a bipolar outflow that implies the presence of an embedded protostellar object within the HH 80N core (GEVWH).

In recent years, observations have found that a number of HH objects have associated molecular condensations. Typically, these clumps are cool ($\sim 10\text{--}20 \text{ K}$), dense ($\gtrsim 3 \times 10^4 \text{ cm}^{-3}$), small (sizes of $\lesssim 0.1 \text{ pc}$ and masses of $\lesssim 1 M_{\odot}$), starless and show little or no evidence of dynamical interaction with the stellar jet (e.g. HH 1/2: Torrelles et al. 1994; Viti et al. 2006; HH 34: Anglada et al. 1995). They are possibly of the same type as the transient small clumps found by Morata et al. (2005) in L673. The high molecular abundances of some species (e.g., CH_3OH , NH_3 , HCO^+) found in these clumps (Girart et al. 2005; Viti et al. 2006) suggest a chemical alteration induced by the UV radiation incoming from the HH object (Taylor & Williams 1996; Viti & Williams 1999; Viti et al. 2003). However, BIMA observations towards the HH 2 region reveal that despite the generally quiescent nature of the molecular condensations ahead of the HH objects, complex dynamical and radiative interactions occur in this region (Girart et al. 2005). The dense core ahead of HH 80N seems to be one of these examples of irradiated cores (Girart et al. 1994, 1998), but it has two peculiarities that make this region an interesting target to study. First, the HH 80N core is significantly larger and more massive than those described above, and shows star formation signatures (GEVWH). This suggests a more complex scenario involving a variety of physical processes. Second, the core shows supersonic infall velocity, which differs from what standard contracting core models predict (e.g. Shu et al. 1987; Basu & Mouschovias 1994; Ciolek &

Mouschovias 1995) or what is observed in other contracting cores (Williams et al. 1999; Belloche et al. 2002; Furuya et al. 2006; Swift et al. 2006). This raises the question whether the outflow has triggered or at least sped up the collapse of the core (GEVWH).

In this work we present the study of the emission of different molecular species observed in the HH 80N core with the BIMA interferometer. Our aim is to characterize the properties of the emission for different molecular tracers and to establish their deviations from the CS (2–1) emission analyzed in GEVWH. We also attempt to provide some possible explanations for the origin of these observed differences by means of a qualitative comparison with other regions, but with special attention to the HH 80N influence. A subsequent analysis of the physical properties as well as a modeling of the chemistry of the core ahead of HH 80N will be reported in a forthcoming paper. In § 2 we present our observations. Their analysis is shown in § 3. In § 4 we discuss the results. Finally, in § 5, we summarize our conclusions.

2. Observations

The 10-antenna BIMA array observations were carried out between November 1999 and May 2001. The phase calibrator used was the QSO J1733–130 and the flux calibrators were Mars, Uranus or Neptune depending on the epoch. A total of 12 frequency setups were used, one at 218.2 GHz and the rest covering frequencies between 85.1 and 109.8 GHz. All the frequency setups were observed in the C configuration apart from the 93.1 GHz frequency setup which was observed in the D configuration. The C configuration had baselines between 6.3 to 100 m, providing an angular resolution of $\sim 5''$ and $\sim 9''$ at 1 mm and 3 mm, respectively. The D configuration had baselines between 6.3 and 30 m, providing an angular resolution of $\sim 25''$ at 3 mm. Each frequency setup has upper and lower frequency bands. The digital correlator was configured to sample part of the 800 MHz wide IF passband in several windows. The typical window for the line observation was configured with a 25 MHz bandwidth and 256 channels, giving a spectral resolution typically of ~ 100 kHz, which corresponds to a velocity resolution of ~ 0.15 km s $^{-1}$ and ~ 0.3 km s $^{-1}$ observing at 1 mm and 3 mm, respectively. For the continuum maps, typical windows of 0.1 GHz divided in 32 channels were used.

The phase tracking center of the observations was set at $\alpha(J2000) = 18^{\text{h}}19^{\text{m}}18^{\text{s}}.618$ and $\delta(J2000) = -20^{\circ}40'55''.00$. The data were calibrated using the MIRIAD package. Maps were made with the visibility data weighted by the associated system temperature and using natural weighting. Different taper functions were used to improve the signal-to-noise ratio depending on the transition. Table 1 lists characteristic parameters of channel as well as continuum emission maps. The table gives the frequency of the transition, the resulting

synthesized beam, the channel resolution and the rms noise of the maps at the channel resolution.

3. Results and analysis

Table 1 lists the transitions (excluding hyperfine components) of all detected molecules: C¹⁸O, HCO⁺, H¹³CO⁺, HCN, CS, SO, N₂H⁺, C₃H₂ and CH₃OH. The Table also lists the transitions of several molecules that were undetected, among them SiO and H₂CO. The 1.4 mm continuum emission was detected marginally with a flux density of 61 ± 16 mJy, peaking at $\alpha(J2000) = 18^{\text{h}}19^{\text{m}}17^{\text{s}}.81$ and $\delta(J2000) = -20^{\circ}40'42''.70$, while no continuum emission was detected at 3.1 mm with an upper limit of ~ 12 mJy beam⁻¹ (at the 3- σ level). Very Large Array 2 cm continuum observations with the D configuration (beamsize $8.1'' \times 4.9''$) do not show emission towards the 1.4 mm continuum peak up to 0.27 mJy beam⁻¹ (at the 3- σ level) (Martí et al. 1993). The combination of 2 cm and 1.4 mm flux density yields $\alpha \geq 2.0$ where α is defined as $S_{\nu} \propto \nu^{\alpha}$, being S_{ν} the flux density at frequency ν . This lower limit value obtained for the spectral index is clearly compatible with having thermal dust emission. Figure 1 shows the integrated emission of the detected lines superimposed on the 8 μm Spitzer image retrieved from the Spitzer archive. For reference, we define the bright central source seen in the 8 μm Spitzer image as the core center ($\alpha(J2000) = 18^{\text{h}}19^{\text{m}}17^{\text{s}}.81$ and $\delta(J2000) = -20^{\circ}40'47''.74$).

As seen in Fig. 1, all the detected molecules (except for N₂H⁺) present an elongated structure with a position angle of $\sim 120^{\circ}$ (i.e. the direction of the major axis) following approximately the same morphology revealed by the dark lane seen in the 8 μm Spitzer image. Clearly, CS is the most extended molecular tracer showing half-power angular dimensions of $60'' \times 25''$. SO, HCN and HCO⁺ behave similarly to CS showing approximately the same angular size, while CH₃OH, C¹⁸O, H¹³CO⁺ and C₃H₂, present smaller sizes, typically $50'' \times 15''$.

Figure 2 shows the channel maps for the different species over the ~ 10.5 to ~ 13.1 km s⁻¹ velocity range, where most of the emission is detected. The 1.4 mm continuum emission is included in the bottom right panel of this figure. The emission of most of the species has a clumpy morphology with different substructures along the core. As mentioned above, GEVWH analyzed the CS (2–1) emission and found that the flattened structure is consistent with a ring-like structure seen edge on. Thus, on basis of this result and for clarity, we divided the core in the different parts of the ring analyzed by GEVWH, plus some other structures.

The features indicated in the first row of Fig. 2 belonging to the ring are: (1) the

eastern side of the ring that appears as a clump seen at 11.0–11.5 km s⁻¹ (hereafter we will call this component East Ring); (2) the western side of the ring, that consists of a clump visible at the same velocities as the East Ring (hereafter, West Ring); (3) the red-shifted side of the ring that is seen at 12 km s⁻¹ as a clump spatially coincident with the core center (hereafter, CR-Ring); (4) in addition, we define the blue-shifted side of the ring at the center of the core as the CB-Ring, seen in 10.52 km s⁻¹ channel. The other features that do not seem to belong to the ring are: (5) the eastern elongated structure found at red-shifted velocities, 12.6–13.1 km s⁻¹, eastwards of the East Ring structure (hereafter, RSE, following the nomenclature used in GEVWH); (6) the northern blue-shifted clump seen only at 11 km s⁻¹ (hereafter, NB). This nomenclature will be followed in the forthcoming analysis.

The inspection of channel maps of Fig. 2 reveals an interesting differentiation between molecular tracers. In addition, the kinematic complexity becomes evident along the major axis of the core. The molecules can be grouped according to the morphology of their emission:

(a) CS, SO and CH₃OH. CS and SO are characterized by having the brightest emission in the East Ring. They also trace other structures such as the West Ring, the NB and the RSE. CH₃OH shows a similar morphology to CS and SO even though its emission is more compact and it is weaker. In particular, the emission of CH₃OH in the RSE and CB-Ring is very marginal.

(b) HCO⁺ and HCN. The strongest emission of these species, especially HCO⁺, arises in the CR-Ring where it shows a prominent clump. In addition, these two species trace the RSE structure. However, the peculiarity of this group of species is that they show little or no emission in the East Ring, unlike the rest of species. The emission of H¹³CO⁺, the optically thin isotopologue of HCO⁺, appears more compact being only significant in the 11.0 to 12.0 km s⁻¹ velocity channels. The H¹³CO⁺ emission is consistent with the HCO⁺ and HCN emission. However, the East Ring shown faintly by HCO⁺ and missed by HCN is clearly traced by H¹³CO⁺. As the two species of this group have a large dipole moment, the lack of emission in the most abundant HCO⁺ isotopologue probably means that there is a foreground cold and low density layer efficiently absorbing their emission (Girart et al. 2000).

The rest of the species exhibit peculiar features and can not be included in any group: the emission of C₃H₂ is quite similar to that of H¹³CO⁺ and traces all the structures except RSE and NB. On the other hand, C¹⁸O only traces the East Ring and the RSE structures. Finally, the N₂H⁺ emission is more compact than the other species not only due to the poor angular resolution, but to the poor signal-to-noise ratio of the observations that would prevent us from detecting any extended emission.

3.1. Analysis of the morphology and kinematics

To better study the kinematic signatures as well as the morphological differences between the detected species, we performed a set of position-velocity (PV) plots along the major (P.A. = 122°) and minor (P.A. = 32°) axis of the core. Subsequently, we analyzed the properties of the emission for the different species by modeling the emission as an optically thin and uniform contracting ring-like structure. This model has been found to fit well the CS emission (GEVWH). The model consists, basically, in a spatially thin disk seen edge-on. A similar model was first used by Ohashi et al. (1997) to study the emission of the contracting core associated with IRAS 04368 + 2557 in L1527. The parameters of our model are the inner and outer radii of the ring, R_{in} and R_{out} , respectively, the infall velocity, V_{inf} , and the intrinsic line width ΔV . Our model does not account for rotation because GEVWH found it to be negligible ($\leq 0.2 \text{ km s}^{-1}$), neither for dynamical infalling, for simplicity. For clarity, we show in Fig. 3 a 3D view of the model geometry. This figure indicates the components of the ring defined in § 3, as well as the directions of minor and major axis. Our strategy is to obtain synthetic PV plots in the minor and major axis of the edge-on ring-like structure, and to compare them with the PV plots taken from the data. Although the ring model is assumed to be spatially thin, we convolved the spatial axis of all the PV plots taken from the model with the angular resolution of our observations. A similar procedure was performed in GEVWH in their attempt to study the CS emission. The authors obtained an inner and outer radii of $R_{\text{in}} = 23''$ and $R_{\text{out}} = 35''$ ($\sim 4 \times 10^4 \text{ AU}$ and $\sim 6 \times 10^4 \text{ AU}$, respectively), an infall velocity of $\sim 0.6 \text{ km s}^{-1}$, and a line width of 0.8 km s^{-1} . In our analysis, we adopted the same model parameters as GEVWH but leaving the inner and outer radii of the ring as free parameters. For consistency, we first analyzed the CS (2–1) data. Once the CS emission is modeled, it becomes a reference for the rest of species. We found a R_{out} of $35''$ ($\sim 6 \times 10^4 \text{ AU}$) and a R_{in} of $15''$ ($\sim 2.5 \times 10^4 \text{ AU}$) being the latter value somewhat smaller than that obtained by GEVWH. For other species, the use of different values of R_{in} and/or R_{out} does not improve significantly the appearance of the residual PV plots. Thus, in those cases we adopted the same R_{in} and R_{out} as for the CS.

Figure 4 shows the PV plots along the major and minor axis of the emission, as well as the residual PV plots after subtracting the best-fit model from the data. As found by GEVWH, the model fits the CS emission reasonably well. However, the PV plots for the other species reveal that they trace the contracting ring-like structure in a non-uniform fashion. The residual PV plots show some of the structures defined above as important features of emission and *absorption* for most species:

- *RSE*. This eastern elongated structure, which is visible in CS, SO, HCO^+ , C^{18}O and marginally in HCN, is clearly independent from the contracting ring as pointed out by

GEVWH. The RSE exhibits a clear linear velocity gradient with increasing velocity toward the east, i.e., as it gets closer to HH 80N.

- *NB*. It is clearly seen in the PV plots along the minor axis of CS, SO and CH₃OH (and marginally C¹⁸O). Due to its position (20'' east from the emission expected from the ring in the minor axis PV plot) this clump is probably independent from the ring structure.
- *East Ring*. It appears as a spot seen in the residual PV plots along the major axis of CS, SO and C¹⁸O (and marginally CH₃OH) located at 11 km s⁻¹ at the eastern part of the ring. Although its position indicates that the East Ring seems to belong to the ring structure, the residual PV plots show that its emission clearly exceeds the emission generated by the uniform ring model.
- *West Ring*. Contrary to the other structures, the West Ring does not show significant emission in the residual PV plots for almost all the species. Only CS, SO and C¹⁸O seem to show marginal emission in the western part of the ring structure. This implies that for the majority of the species the molecular emission is consistent with the emission expected for the ring model in this part of the ring.
- *CR-Ring*. The CR-Ring seems to be physically part (at least partially) of the ring structure but it exhibits stronger emission than that expected from the ring model for HCN and, especially HCO⁺, as clearly seen in the residual PV plots.
- *CB-Ring*. This structure is visible as negative contours in the residual PV plots for the major and minor axis for most of the species. The CB-Ring component is best traced by CS, but presents an important lack of emission for the rest of species, being most evident for HCO⁺.

3.2. Relative abundances

Table 2 lists the positions that we consider most representative of the structures defined previously. Figure 5 shows the spectra of the detected transitions taken at the five selected positions shown in Table 2. Note that some of the spectra taken at the center of the core present two velocity components, separated by ~ 1 km s⁻¹. This result, especially evident for CS, is perfectly compatible with the contracting ring-like morphology found previously for the core and, in fact, these two velocity components appear to coincide with the CB-Ring and CR-Ring components. Another general feature is that the spectra show narrow linewidths, with a FWHM ranging from 0.6 to 1.4 km s⁻¹, which indicates that the gas in

the cores is not shocked (typical linewidths found in shocked regions are 6-7 km s⁻¹, e.g. Bachiller et al. 1995).

From the spectra of Fig. 5 we derived the column densities in all the components. To do so, we used RADEX, a non-LTE excitation and radiative transfer code that can provide us constraints on the gas density, kinetic temperature and/or the column density (van der Tak et al. 2007). RADEX was used adopting the temperature of 17 K, which is close to the rotational temperature obtained from ammonia (Girart et al. 1994). We used the HCO⁺ (3–2) and H¹³CO⁺ (3–2) lines observed by Girart et al. (1998) in combination with the H¹³CO⁺ (1–0) (smoothed to the CSO angular resolution) of our dataset to constrain the range of possible values for the average gas density. We calculated line intensity ratios of these lines assuming a comparable beam dilution. Then, we ran the code to explore the densities that yield brightness temperatures ratios compatible with our measured values (within a 20 per cent range due to uncertainties).

We found a possible range of $5 \times 10^4 - 1.3 \times 10^5$ cm⁻³ for the average gas density in the core. Once the density range is constrained and the kinetic temperature fixed, using RADEX again we were able to search for the column density range that yields the line intensities measured in the spectra of Fig. 5. For HCO⁺, the column density was derived using the optically thin isotopologue H¹³CO⁺ and adopting a carbon isotope abundance ratio, C¹²/C¹³, of 63 (Langer & Penzias 1990; 1993). The results are presented in Table 3.

In order to clarify the scenario that leads to the chemical properties observed in each structure we computed the relative abundances with respect to CS. The reason for adopting such a scale is that CS appears to be the most fiducial molecule since its chemistry seems to be directly related to dense gas. In fact, it is the molecule that more regularly traces the contracting edge-on ring. In addition, as the lines involved in this analysis were taken with the same configuration and beam sizes, then the missing flux effects are probably canceled out. Another advantage of using the molecular abundances relative to CS is that most of the observed transitions have a high critical density similar to CS (2–1) and, hence, they trace approximately the same gas (with the possible exception of C¹⁸O). The resulting ranges of fractional abundances with respect to CS corresponding to the density range derived above are shown in Table 4.

We also calculated the logarithmic median and the standard deviation of the relative abundances for the same molecules detected in the HH 80N clump over a sample for three types of environments related with dense gas found in the bibliography: molecular clumps associated with HH objects, low-mass star-forming cores and dark molecular clouds. Figure 6 shows the comparison of the fractional abundances of these three types of environments with the values of Table 4 (see figure caption for information on the sources of these samples).

The description of the chemical properties seen in Fig. 6 led us to classify the observed molecules depending on the variability of their relative abundances between the different components of the core:

(a) $C^{18}O$ is the molecule that presents the major variability between components. It exhibits a high relative abundance with respect to CS towards RSE (between a factor of 2 to 5 with respect to the rest of components) although it is undetected or has low relative abundances in the rest of the components.

(b) SO, CH_3OH and HCO^+ have abundances higher than CS but presents a moderate variability. The comparison between their relative abundances with respect to CS in the different components of the core for the different species in this group never exceeds a factor of 3. There is, however, a difference between the molecules in this group: while SO and CH_3OH relative abundances are maximum at the East Ring position, HCO^+ presents the highest abundances towards CR-Ring and West Ring.

(c) C_3H_2 and HCN exhibit a moderate variability and each molecule shows a distinct behavior. Clearly, C_3H_2 is poorly detected along the core. On the other hand, as seen in § 3, HCN has a similar morphology as HCO^+ . Since both molecules have comparable dipole moments, the HCN emission may be considerably self-absorbed, similarly as HCO^+ . Therefore, HCN relative abundances are likely underestimated in most components of the core.

4. Discussion

4.1. Star formation activity within the core

This work presents the results of a molecular survey carried out with BIMA towards the star forming core ahead of HH 80N, for which the CS and CO data were already reported in GEVWH. From the CS data, GEVWH detected an elongated dense core with 0.24 pc of radius seen edge on. The properties of the CS emission suggested that it was tracing a ring structure contracting with a striking supersonic infall velocity (0.6 km s^{-1}). The central 'hole' of the ring is presumably the result of molecular depletion due to the high central density that might be reached in this core. From the CO data, GEVWH found a bipolar outflow that is a signpost of an ongoing star forming process in the core. The Spitzer $8 \mu\text{m}$ and the BIMA 1.4 mm dust images show a bright source located at the center of the bipolar CO outflow. This strongly suggests the presence of an embedded protostellar object within the core, which powers the bipolar outflow.

The CS emission was used in GEVWH to derive the mass of the ring structure. Their obtained value, which is $12 M_{\odot}$ assuming $X(\text{CS}) = 2 \times 10^{-9}$ ($10 M_{\odot}$ belonging to the main core, and $2 M_{\odot}$ to RSE), is somewhat lower than the value obtained from NH_3 ($20 M_{\odot}$, Girart et al. 1994). The 1.4 mm continuum emission is barely resolved, which implies that it arises from a region with a size of $\sim 10^4$ AU in diameter. The mass of the dust can be estimated using the formula

$$M_d = \frac{S_{1.4} D^2 c^2}{2kT_d \nu^2 k_{1.4}} \quad (1)$$

where $S_{1.4}$ is the continuum flux measured at 1.4 mm, D is the distance to the source, T_d is the dust temperature, and $k_{1.4}$ is the mass opacity coefficient at 1.4 mm. In our calculations we assume a $k_{1.4}$ of $0.83 \text{ cm}^2 \text{ gr}^{-1}$ obtained from $k_{1.3}$ for a density of $n_{\text{H}_2} \simeq 10^6 \text{ cm}^{-3}$ (Col. 2 in Table 2 of Ossenkopf & Henning 1994) and assuming a dust opacity index of 2, and a temperature range of 20–40 K (Jennings et al. 1987), which is among the temperatures expected from classical theoretical models of protostellar envelopes (e.g. Adams & Shu 1985). Note that this expression uses the Rayleigh-Jeans approximation, valid at millimeter wavelengths. For our values the mass of the dust is $0.019\text{--}0.036 M_{\odot}$. Adopting a gas-to-dust ratio of 100, the total mass of the envelope traced by the dust emission is $1.9\text{--}3.6 M_{\odot}$.

Bontemps et al. (1996) found a relationship between the outflow momentum flux, the envelope mass and the bolometric luminosity. GEVWH found that the envelope mass was almost an order of magnitude higher than the values predicted by Bontemps et al., for the measured CO momentum flux. However, Bontemps et al. derived the mass of the envelope for the sources in their sample by integrating the 1.3 mm emission over a region corresponding to ~ 0.05 pc (10^4 AU), whereas GEVWH used the mass derived from the CS emission, which traces a region with a radius of 0.24 pc. The derived mass from the 1.4 mm dust corresponds to a region of size approximately similar to that used in Bontemps et al. Thus, if we use the total mass of the envelope derived from the 1.4 mm flux, then the relationship between the envelope mass and the CO outflow momentum flux fits very well.

The study of the circumstellar mass surrounding the YSOs at several radii is a useful tool to track their evolution (André & Montmerle 1994). Class 0 YSOs are best interpreted as very young protostars whose dense circumstellar envelope still contains an important reservoir of mass to be accreted. Therefore the fact that the bulk of the mass of the HH 80N core is found at large radii from its central embedded YSO suggests that this object should be at the beginning of the main accretion phase and, hence, it is another signpost of being an extremely young YSO found probably in the Class 0 stage (e.g. Girart et al. 2009).

4.2. Chemical properties

The analysis of the other species of the molecular survey confirms that their morphology roughly follows the ring-like morphology seen in CS, contracting with a supersonic infall velocity ($\sim 0.6 \text{ km s}^{-1}$), though this is a first-order result: a more accurate analysis reveals that most of the molecular species, although tracing approximately the same region as CS, show important local differences. This deviation reflects a possible combination effect of excitation, optical depth and molecular abundance, being the latter the most plausible candidate to explain most of the observed differences.

In this section, we attempt a simple discussion on the possible origin of the observed differentiation by means of a qualitative comparison with the chemistry observed in several environments associated with the dense gas. We investigate whether the chemistry observed in the HH 80N core is the result of a strong central depletion and of photochemical effects caused by the UV radiation coming from the HH 80N object, as pointed out by GEVWH.

4.2.1. *The ring-like morphology and the central depletion*

As suggested by GEVWH, the ring-like structure is likely due to the freeze-out of the molecules onto the dust grains at the inner regions of the core, where high densities are expected. In addition, there is a young protostellar object embedded in the core. Thus, the conditions of the central part of the core should resemble those found in protostellar cores. In this section we analyze the inner structure of the core by comparing it qualitatively with other similar regions.

When modeling the radial variation of molecular abundances in a circumstellar envelope one has to take into account the effects of the central embedded YSO, heating the inner part of the core, which causes partial sublimation of the icy dust mantles (e.g. IRAS 16293-2422: Ceccarelli et al. 2000; Schöier et al 2002; NGC1333: Maret et al. 2002, 2004; Jørgensen et al. 2005; Bottinelli et al. 2007). However, we do not see any signpost of a warm component (temperatures of several tens of K) in the HH 80N core, which could be due to either the low luminosity or the youth of the YSO, as well as the distance of the region (in other words, the expected warm region is likely highly beam diluted).

Outside the undetected warm inner region, the HH 80N core exhibits a large region where molecules seem to be strongly frozen in the icy mantles, except possibly for NH_3 (Girart et al. 1994) and N_2H^+ , molecules that seem to exhibit a more compact emission. Unfortunately, from the analysis of the PV plots we are not able to determine whether other species deplete at different radii from the center of the core than that of CS. In any case,

the depletion radius of the HH 80N core ($\sim 2.5 \times 10^4$ AU) is significantly larger (by 3–4 times) than those obtained for prestellar cores by Tafalla et al. (2006). Because the densest gas traced by molecular species is expected to be found at the inner radius of the ring, the lower value of the possible range of average densities for the HH 80N core found in § 3.2 ($5 \times 10^4 \text{ cm}^{-3}$) can be taken as a lower limit for the density at the depletion radius (i.e. depletion density). As the Class 0 object forming inside the HH 80N core is very young, the core probably still retains the initial conditions for star formation. Hence, there might be some physical connection with the prestellar cores, specially with those that are found on the verge of dynamical collapse. The CS is depleted at densities of the order of a few 10^4 cm^{-3} in prestellar cores (Tafalla et al. 2002; Pagani et al. 2005), slightly below the lower limit for the depletion density in the HH 80N core. The large depletion radius and densities found for the HH 80N core suggests high central densities. This could be due to a more evolved stage of the HH 80N core with respect to prestellar cores, favored by its rapid collapse.

Surrounding the ‘frozen’ region, the HH 80N core has a molecular shell or ring-like structure. Since a minimum gas density is required to observe a given molecular transition, the detection of some specific transitions of our dataset can provide an estimation of the lower possible densities of this shell (i.e. at outer radius 6×10^4 AU). In particular, the detection of HCO⁺ (1–0) line implies densities higher than $2.4 \times 10^3 \text{ cm}^{-3}$ (for which this transition is easily detectable, Evans et al. 1999). In summary, we conclude that the densities traced by the molecular emission associated with the ring-like structure are above $\sim 2 \times 10^3 \text{ cm}^{-3}$, reaching values likely higher than $5 \times 10^4 \text{ cm}^{-3}$ at the inner radius.

4.2.2. *The components of the ring-like structure*

In Figure 3 we present the most likely scenario as seen by an hypothetical observer. In the following we analyze the enhancement of some species on the basis of this scenario and in the frame of the UV irradiation. Our main consideration is the effect of the distance of each component with HH 80N. The fact that HH 80N may not lie in the same plane of sky as the core does not affect qualitatively our analysis. This picture implies higher photochemical activity in the East Ring and moderate or low photochemical effects for the CR-Ring, West Ring and CB-Ring. In particular, Table 3 shows that the column densities of CS, CH₃OH, C¹⁸O and SO follow fairly well this trend: most of them are higher in the East Ring than in the West Ring.

One of the most evident results of Fig. 6 is that the enhancement of SO in the East Ring component (the closest in projection to HH 80N) resembles that obtained for the clump ahead of the HH 2 jet (Girart et al. 2005) and determined to be due to chemical effects induced

by an enhanced radiation field. This trend is also observed for CH_3OH and C^{18}O . Figure 7 also shows that SO and CH_3OH are higher than the typical range of values of low mass star forming cores. The caveat to this scenario is HCO^+ , which presents similar column densities in all the components of the ring (with the exception of CB-Ring) instead of being greater in the East Ring and CR-Ring, as one would expect if the radiation field impinging on the ring were higher than the interstellar radiation field. This result indicates that other parameters, apart from the effect of the distance to HH 80N, also play a role on the chemistry of the core. Clearly, a detailed modeling, which is however beyond the scope of this paper, is required in order to characterize the chemistry of the core ahead of HH 80N.

Molinari et al. (2001), using a simple model, derived a value of $670 G_0$ for the FUV field emanating from the recombination region in HH 80N. From this value, only the fraction of photons that impinges to the HH 80N core over the total has to be taken in account. Taking 0.2 pc as the distance between the core and the HH object, and assuming that the core is seen edge on from HH 80N, we obtain a dilution factor of $1/16$, which yields $\sim 40 G_0$ for the side of the core facing HH 80N (the East Ring). Interestingly, this value is within the range of possible values for the radiation field expected to impinge the clump ahead of HH 2 (Viti et al. 2003). However, note that the dilution factor derived above is based on a projected distance. Therefore, its value as well as the estimated FUV are upper limits.

On the other hand, based on the range of average density values estimated in § 3.2, the derived column density through the ring seen from the edge of the core is $N(\text{H}_2) = 2.5 - 6.5 \times 10^{22} \text{ cm}^{-2}$. Then, the derived the visual extinction, A_v , from the relationship $N(\text{H}_2) \simeq 10^{21} A_v$ (Spitzer 1978) is between 25–65 mag, much greater than the values where the photochemical effects are attenuated (e.g. Viti & Williams 1999). Although HH 80N does not lie exactly on the same plane of the ring, these high extinction values are only approximate and indicate that the UV photons hardly penetrate deep inside the core. Therefore, any photochemical effects that may affect the East Ring are likely to happen on the "surface" of the ring.

The decrease of photochemical activity in the parts of the ring further away than the East Ring is possibly a combined effect of geometrical dilution and the presence of a low density cloud component. In fact, the distance from HH 80N to the western parts of the ring is a factor of 2–3 greater than that to the illuminated side (~ 0.2 pc), and much larger than the typical distances between other HH objects and their respective associated clumps (~ 0.05 pc, Viti et al. 2006).

4.2.3. Other molecular clumps in the region

The RSE and NB structures were poorly detected in the species of our survey. Both structures appear to be spatially independent from the ring structure in addition of being smaller. Therefore, these components may present different chemistry simply because their basic physical structure might be different from the physical structure of the ring. There is, however, an important difference between RSE and NB: while $C^{18}O$ exhibits a high relative abundance with respect to CS in RSE reaching values typical of those found in the HH 2 region (I4 position), it is undetected in NB. In addition, HCO^+ is not enhanced with respect standard molecular cloud values in NB, implying that the UV radiation does not play a significant role in the chemistry of this structure.

5. Conclusions

We have carried out an observational study with the BIMA array of the star forming dense core ahead of HH 80N in order to characterize its morphological and chemical properties. We present maps of the different molecular species detected with BIMA (CS , HCO^+ , $H^{13}CO^+$, HCN , CH_3OH , SO , $C^{18}O$, and C_3H_2) as well as 1.4 mm continuum dust emission. These maps reveal a complex morphology and kinematics for this core. In an attempt to understand this complexity, we obtained PV plots for all the species along the major and minor axis of the core and modeled them in a similar procedure as in GEVWH. Subsequently, we derived the column density and the relative abundances with respect to CS in some selected positions along the core. Our main conclusions can be summarized as follows:

1. The 1.4 mm dust emission was detected marginally in a position close to the Spitzer $8 \mu m$ source. This source is located at the center of the CO bipolar outflow found by GEVWH and, therefore, it is likely its powering source. The 1.4 mm dust emission traces the inner and denser region ($\lesssim 10^4$ AU) of the dense core around the protostar. The mass of the dense core ($1.9\text{--}3.6 M_\odot$) at scales up to $\simeq 10^4$ AU and the momentum flux of the CO bipolar outflow correlate well with what is expected for very young Class 0 sources (Bontemps et al. 1996).
2. The integrated emission for most of the molecular tracers reveals a clumpy and elongated morphology with a size of $\sim 60'' \times 25''$ ($0.5 \text{ pc} \times 0.2 \text{ pc}$) and a position angle of $\sim 120^\circ$. Three main structures can be distinguished: the central core around the protostar and two smaller clumps (RSE and NB). As previously observed in CS by GEVWH, the molecular emission associated with the central core arises from the outer shell of the dense core. This molecular shell has a ring-like morphology seen edge-on, which is

well-traced by CS and partially traced by the other molecular species. The inner and outer radii of the ring are $\sim 2.5 \times 10^4$ AU and $\sim 6.0 \times 10^4$ AU, respectively, and the estimated averaged density ranges between $5 \times 10^4 \text{ cm}^{-3}$ and $1.3 \times 10^5 \text{ cm}^{-3}$. The ring structure has been divided in four regions, following the CS clumpy morphology: the East Ring, Central Red-shifted Ring (CR-ring), the Central Blue-shifted Ring (CB-ring) and the West Ring. The kinematics traced by the different molecules are similar to that found for CS by GEVWH, which is indicative of contraction with a supersonic infall velocity of 0.6 km s^{-1} .

3. The relative abundances with respect to CS derived in different positions were compared with those obtained for a sample of dark clouds, low-mass star-forming cores and other molecular clumps ahead of HH objects. This comparison suggests that the relative abundances of SO, C¹⁸O and, to a lesser extent CH₃OH, are partially compatible with the high level of UV irradiation generated by HH 80N. In particular, the section of the molecular ring facing HH 80N (East Ring), as well as RSE, seem to be the regions more exposed to the UV radiation, whereas in the other sections of the ring and NB the photochemical effects seem to be less important. The molecular ring has a visual extinction, A_v , between 25 and 65 mag seen from the edge. These values are much higher than the maximum extinction at which the UV radiation can effectively penetrate the ring and release the molecular species from the dust mantles triggering the photochemistry (Viti et al. 2003). Inside the molecular ring, at scales of $\lesssim 2.5 \times 10^4$ AU, where extremely high densities are found, the dense core exhibits a “frozen” region, where the observed molecules are significantly depleted onto icy dust mantles.

We thank the anonymous referee for his valuable comments, which helped to improve the paper. JMG, RE, MBT and JMM are supported by MEC grant AYA2005-05823-C03 (co-funded with FEDER funds). JMG and JMM are partially supported by AGAUR grant 2005 SGR 00489. SV acknowledges financial support from an individual STFC (ex-PPARC) Advanced Fellowship.

REFERENCES

- Adams, F. C., & Shu, F. H. 1985, *ApJ*, 296, 655
 André, P., & Montmerle, T. 1994, *ApJ*, 420, 837

- Anglada, G., Estalella, R., Mauersberger, R., Torrelles, J. M., Rodríguez, L. F., Cantó, J., Ho, P. T. P., & D'Alessio, P. 1995, *ApJ*, 443, 682
- Bachiller, R., Liechti, S., Walmsley, C. M., & Colomer, F. 1995, *A&A*, 295, L51
- Basu, S., & Mouschovias, T.C. 1994, *ApJ*, 432, 720
- Belloche, A., André, P., Despois, D., & Blinder, S. 2002, *A&A*, 393, 927
- Blake, G. A., Sandell, G., van Dishoeck, E. F., Groesbeck, T. D., Mundy, & L. G., Aspin, C. 1995, *ApJ*, 441, 689
- Bontemps, S., Andre, P., Terebey, S., & Cabrit, S. 1996, *A&A*, 1996, 311, 858
- Bottinelli, S, Ceccarelli, C., Williams, J. P., & Lefloch, B. 2007, *A&A*, 463, 601
- Ceccarelli, C., Castets, A., Caux, E., Hollenback, D., Loinard, L., Molinari, S., & Tielens, A. G. G. M. 2000, *A&A*, 355, 1129
- Ciolek, G. E., & Mouschovias, T. C. 1995, *ApJ*, 454, 194
- di Francesco, J., Hogerheide, M. R., Welch, W. J., & Bergin, E. A. 2002, *AJ*, 124, 2749
- Evans, N. 1999, *ARA&A*, 37, 311
- Furuya, R. S., Kitamura, Y., & Shinnaga, H. 2006, *ApJ*, 653, 1369
- Girart, J.M., et al. 1994, *ApJ*, 435, L145
- Girart, J. M., Estalella, R., & Ho, P. T. P. 1998, *ApJ*, 495, L59
- Girart, J. M., Estalella, R., Ho, P. T. P., & Rudolph, A. L. 2000, *ApJ*, 539, 763
- Girart, J. M., Estalella, R., Viti, S., Williams, D. A., & Ho, P. T. P. 2001, *ApJ*, 562, L91
- Girart, J. M., Viti, S., Estalella, & Williams, D. A. 2005, *A&A*, 439, 601
- Girart, J. M., Rao, R., & Estalella, R. 2009, *ApJ*, in press (arXiv:1108.3415)
- Jennings, R. E., Cameron, D. H. M., Cudlip, W., & Hirst, C. J. 1987, *MNRAS*, 226, 461
- Jørgensen, J. K., Schöier, F. L., & van Dishoeck, E. F. 2004, *A&A*, 416, 603
- Jørgensen, J. K., Bourke, T. L., Myers, P., Schöier, F. L., van Dishoeck, E. F., & Wilner, D. J. 2005, *ApJ*, 632, 973
- Langer, W. D., & Penzias, A. A. 1990, *ApJ*, 357, 477
- Langer, W. D., & Penzias, A. A. 1993, *ApJ*, 408, 539
- Maret, S., Ceccarelli, C., Tielens, A. G. G. M., Caux, E., & Castets, A. 2002, *A&A*, 395, 573
- Maret, S., et al. 2004, *A&A*, 416, 577

- Maret, S., Ceccarelli, C., Tielens, A. G. G. M., Caux, E., Lefloch, B., Faure, A., Castets, A., & Flower, D. R. 2005, *A&A*, 442, 527
- Martí, J., Rodríguez, L. F., & Reipurth, B. 1993, *ApJ*, 416, 208
- Molinari, S., Noriega-Crespo, A., & Spinoglio, L. 2001, *ApJ*, 547, 292
- Morata, O., Girart J. M., & Estalella, R., 2005 *A&A*, 435, 113
- McMullin, J. P., Mundy, L. G., & Blacke, G. A. 1994, *ApJ*, 437, 305
- McMullin, J. P., Mundy, L. G., Blacke, G. A., Wilking, B. A. Mangum, J. G., & Latter, W. B. 2000, *ApJ*, 536, 845
- Ohashi, N., Hayashi, M., Ho, P. T. P., & Momose, M. 1997, *ApJ*, 475, 211
- Ossenkopf, V., & Henning, T. 1994, *A&A*, 291, 943
- Pagani, L., Pardo, J. -R., Apponi, A. J., Bacmann, A., & Cabrit, S. 2005, *A&A*, 429, 181
- Pratap, P., Dickens, J. E., Snell, R. L., Miralles, M. P. Bergin, E. A. Irvine, W. M., & Schloerb, F. P. 1997, *ApJ*, 486, 862
- Reipurth, B., & Graham, J. A. 1988, *A&A*, 202, 219
- Rodríguez, L. F., Moran, J. M., Gottlieb, E. W., & Ho, P. T. P. 1980, *ApJ*, 235, 845
- Schöier, F. L., Jørgensen, J. K., van Dishoek, E. F., & Blacke, G. A. 2002, *A&A*, 390, 1001
- Shu, F. H., Adams, F. C., & Lizano, S. 1987, *ARA&A*, 25, 23
- Spitzer, L. 1978, *Physical Processes in the Interstellar Medium* (New York: Wiley)
- Swift, J., Welch, W. J., di Francesco, J. D., & Stojimirović, I. 2006, *ApJ*, 637, 392
- Tafalla, M., Myers, P. C., Caselli, P., Walsmley, C. M., & Comito, C. 2002, *ApJ*, 569, 815
- Tafalla, M., Santiago-Garcia, J., Myers, P. C., Caselli, P., Walmsley, C. M., & Crapsi, A. 2006, *A&A*, 455, 577
- Taylor, S.D., & Williams, D.A. 1996, *MNRAS*, 282, 1343
- Torrelles, J. M., Gómez, J. F., Ho, P. T. P., Rodríguez, L. F., Anglada, G., & Cantó, J. 1994, *ApJ*, 435, 290
- Ungerechts, H., Bergin, E. A., Goldsmith, P. F., Irvine, W. M., Schloerb, F. P., & Snell, R. L. 1997, *ApJ*, 482, 245
- van der Tak, F. F. S., Black, J. H., Schöier, F. L., Jansen, D. J., & van Dishoek, E. F. 2007, *A&A*, 468, 627
- van Dishoek, E. F., Blake, G. A., Geoffrey, A., Jansen, D. J., & Groesbeck, T. D. 1995, *ApJ*, 447, 760

Viti, S., & Williams, D. A. 1999, MNRAS, 310, 517

Viti, S., Girart, J. M., Garrod, R., Williams, D. A., & Estalella, R. 2003, A&A, 399, 187

Viti, S., Girart, J. M., & Williams, D. A. 2006, A&A, 449, 1089

Williams, J. P., Myers, P. C., Wilner, D. J., & di Francesco, J. 1999, ApJ, 513, L61

Table 1: Characteristic values of BIMA channel maps.

Transition	ν GHz	Configuration	Beam ^a arcsec \times arcsec	PA degrees	rms (Jy beam ⁻¹)	Δv_{ch} (km s ⁻¹)	Peak emission ^b (Jy beam ⁻¹)
HCO ⁺ (1–0)	89.1885	C	14.1 \times 6.9	1.2	0.13	0.33	3.65
HCN (1–0)	88.6319	C	14.2 \times 6.7	1.7	0.13	0.33	1.55
C ₃ H ₂ (2 _{1,2} –1 _{0,1})	85.3389	C	14.7 \times 7.0	1.8	0.13	0.34	0.87
CS (2–1)	97.9810	C	15.6 \times 7.1	3.0	0.18	0.30	2.36
C ¹⁸ O (1–0)	109.7822	C	13.9 \times 6.5	–2.9	0.29	0.27	2.77
SO (2 ₃ –1 ₂)	109.2522	C	14.2 \times 6.6	–2.0	0.24	0.40	≤ 0.72
SO (2 ₁ –1 ₁)	86.7543	C	18.1 \times 7.8	0.6	0.15	0.58	≤ 0.45
SO (3 ₂ –2 ₁)	99.2999	C	15.6 \times 7.2	0.7	0.21	0.29	3.05
SO (5 ₅ –4 ₄)	215.2207	C	7.8 \times 3.8	–2.4	0.93	0.41	≤ 2.79
CH ₃ OH (2 _n –1 _n)	96.7414 ^c	C	16.9 \times 7.5	–6.0	0.18	0.30	1.33
N ₂ H ⁺ (1–0)	93.1738 ^d	D	32.1 \times 18.8	10.0	0.73	0.16	6.01
H ¹³ CO ⁺ (1–0)	86.7543	C	16.2 \times 7.6	2.0	0.16	0.34	0.99
C ₂ S (6 ₇ –5 ₆)	86.1841	C	17.2 \times 7.9	1.1	0.12	0.58	≤ 0.36
SiO (2–1)	86.8461	C	18.1 \times 7.9	–0.8	0.12	0.32	≤ 0.36
HCOOH (4 _{0,4} –3 _{0,3})	89.5792	C	17.6 \times 7.8	–0.9	0.16	0.55	≤ 0.48
H ₂ CS (3 _{0,3} –2 _{0,2})	103.0404	C	14.5 \times 6.2	2.0	0.15	0.57	≤ 0.45
H ₂ CO (3 _{0,3} –2 _{0,2})	218.2222	C	7.7 \times 3.7	–9.5	0.94	0.40	≤ 2.82
Continuum (1.4 mm)	217.0	C	7.3 \times 3.0	–4.5	0.016	—	0.061
Continuum (3.1 mm)	99.5	C	15.5 \times 6.8	–6.7	0.004	—	≤ 0.012

^aA taper function of 4'' was used in all the channel maps except for C¹⁸O(1–0) (2.0''), SO(5₅–4₄) (2.5''), SiO(2–1) (2.0''), H₂CS(3₀₃–2₀₂) (2.0''), H₂CO(3₀₃–2₀₂) (2.5'') and continuum (1.4 mm) (1.0'') maps.

^b Upper limits are 3 times the rms.

^c Frequency for the 2₀–1₀–A line. The 2_{–1}–1_{–1}–E line was also detected.

^d Frequency for the F₁ F=2₃–1₂ hyperfine line. All the hyperfine 1–0 components were detected.

Table 2: Representative positions.

Structure	Position		Map counterpart ^a
	α (J2000)	δ (J2000)	
RSE	18 ^h 19 ^m 21 ^s .10	–20°41′15″.0	CS (2–1) > 12 km s ^{–1} eastern elongation
NB	18 ^h 19 ^m 18 ^s .10	–20°40′26″.9	CS (2–1) 11 km s ^{–1} northern peak
East Ring	18 ^h 19 ^m 19 ^s .03	–20°40′53″.0	SO (3 ₂ –2 ₁) 11 km s ^{–1} eastern peak
CB-Ring & CR-Ring	18 ^h 19 ^m 17 ^s .81	–20°40′47″.7	HCO ⁺ (1–0) 12 km s ^{–1} center peak
West Ring	18 ^h 19 ^m 16 ^s .57	–20°40′31″.5	CS (2–1) 11 km s ^{–1} western peak

^aMolecule used to better highlight the structure.

Table 3: Column densities^a (in units of 10¹³ cm^{–2})

Molecule	CS		SO		CH ₃ OH ^b		HCN		HCO ⁺ ^d		C ₃ H ₂		C ¹⁸ O	
	N_m	N_M	N_m	N_M	N_m	N_M	N_m	N_M	N_m	N_M	N_m	N_M	N_m	N_M
RSE	0.9	0.5	1.2	0.7	≤ 1.8 ^c	≤ 2.1 ^c	0.6	0.3	≤ 2.5 ^c	≤ 1.8 ^c	≤ 0.2 ^c	≤ 0.1 ^c	171	180
NB	2.2	1.0	2.1	1.1	≤ 3.0 ^c	≤ 3.4 ^c	≤ 1.0 ^c	≤ 0.5 ^c	≤ 2.2 ^c	≤ 1.6 ^c	≤ 0.5 ^c	≤ 0.2 ^c	≤ 154 ^c	≤ 162 ^c
East Ring	4.6	2.4	13.6	6.4	10.0	11.4	1.8	0.7	7.2	5.1	0.8	0.4	280	293
CB-Ring	1.2	0.7	2.1	1.2	≤ 2.6 ^c	≤ 2.9 ^c	≤ 1.2 ^c	≤ 0.5 ^c	≤ 4.8 ^c	≤ 3.4 ^c	≤ 0.5 ^c	≤ 0.3 ^c	≤ 123 ^c	≤ 130 ^c
CR-Ring	2.8	1.5	3.1	1.7	2.7	3.1	6.6	2.2	6.9	4.7	0.5	0.2	≤ 123 ^c	≤ 130 ^c
West Ring	4.1	2.1	8.7	4.0	5.1	5.8	6.2	2.2	9.1	6.0	1.0	0.5	166	175

^a N_m and N_M are the column densities derived for the lower (5×10^4 cm^{–3}) and upper (1.3×10^5 cm^{–3}) values of the density range derived from the RADEX analysis (see § 3.2)

^b Including CH₃OH-A and CH₃OH-E.

^c Upper limits are 3 times the rms noise.

^d Derived from H¹³CO⁺.

Table 4: Relative abundances with respect to CS^a

Molecule	SO		CH ₃ OH ^b		HCN		HCO ⁺		C ₃ H ₂		C ¹⁸ O	
	X_m	X_M	X_m	X_M	X_m	X_M	X_m	X_M	X_m	X_M	X_m	X_M
RSE	1.3	1.3	≤ 2.0 ^c	≤ 4.0 ^c	0.7	0.5	≤ 2.7 ^c	≤ 3.4 ^c	≤ 0.2 ^c	≤ 0.2 ^c	190	346
NB	1.0	1.1	≤ 1.4 ^c	≤ 3.3 ^c	≤ 0.5 ^c	≤ 0.4 ^c	≤ 1.0 ^c	≤ 1.6 ^c	≤ 0.2 ^c	≤ 0.2 ^c	≤ 72 ^c	≤ 157 ^c
East Ring	3.0	2.7	2.2	4.8	0.4	0.3	1.6	2.2	0.2	0.2	61	125
CB-Ring	1.7	1.7	≤ 2.1 ^c	≤ 4.1 ^c	≤ 1.0 ^c	≤ 0.7 ^c	≤ 4.0 ^c	≤ 4.8 ^c	≤ 0.5 ^c	≤ 0.4 ^c	≤ 103 ^c	≤ 183 ^c
CR-Ring	1.1	1.2	1.0	2.1	2.4	1.5	2.5	3.2	0.2	0.2	≤ 45 ^c	≤ 89 ^c
West Ring	2.1	1.9	1.3	2.7	1.5	1.0	2.2	2.8	0.3	0.2	40	83

^a X_m and X_M are the abundance values derived for the lower (5×10^4 cm^{–3}) and upper (1.3×10^5 cm^{–3}) limits of the density range derived from the RADEX analysis (see § 3.2).

^b Including CH₃OH-A and CH₃OH-E.

^c 3-sigma upper limits.

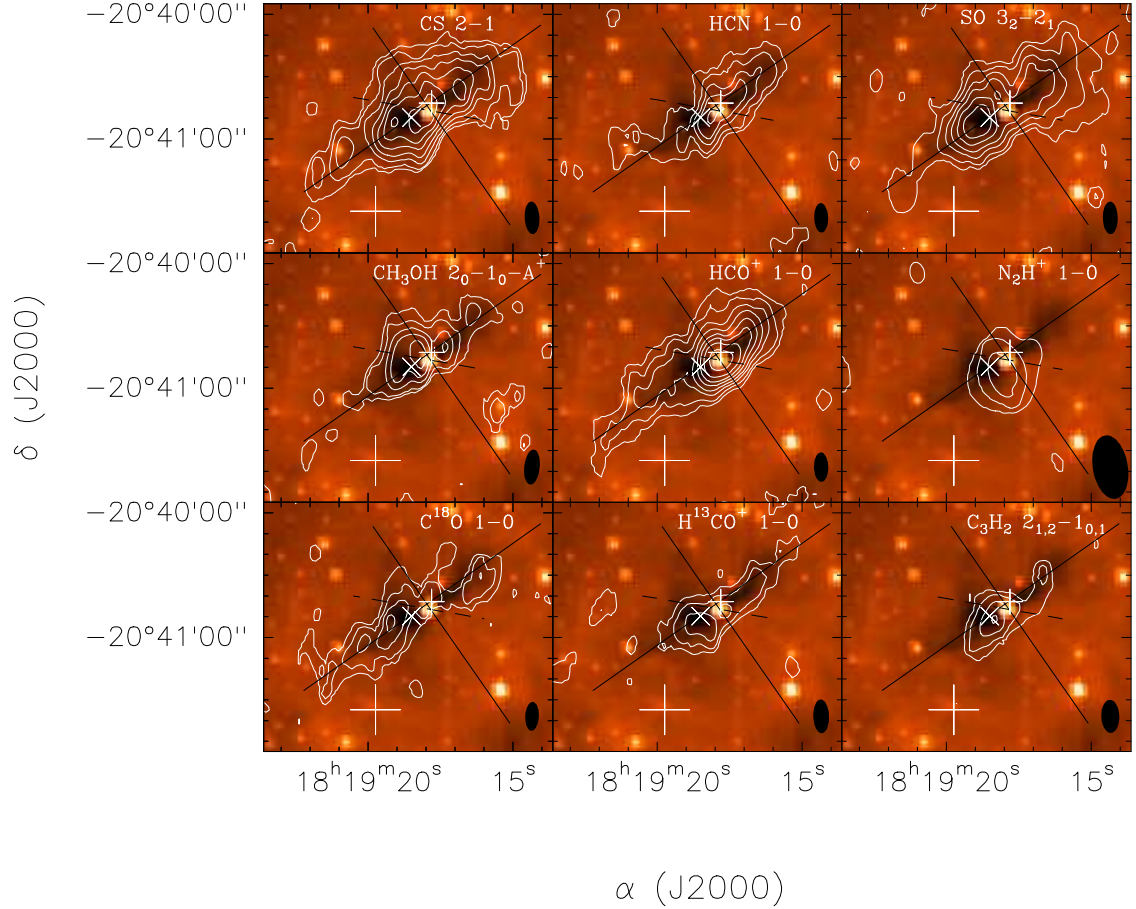


Fig. 1.— Superposition of the Spitzer image ($8 \mu\text{m}$; color scale) and the zero-order moment (integrated emission; white contours) over the $9.5\text{--}14.09 \text{ km s}^{-1}$ velocity range, of the species detected with BIMA in the HH 80N core. The Spitzer image shows the HH 80N core in absorption against the background emission. The contour levels are 2, 4, 7, 10, 14, 18, 23, and 30 times the rms of each map: 0.14 (CS and SO), 0.11 (HCN, CH_3OH and HCO^+), 0.1 (H^{13}CO^+ and C_3H_2), 0.17 (C^{18}O) and 0.40 (N_2H^+) $\text{Jy beam}^{-1} \text{ km s}^{-1}$. The beam is shown in the bottom right corner of each panel. The large and small crosses mark the HH 80N object and the continuum peak at 1 mm , respectively. The tilted cross marks the NH_3 peak (Girart et al. 1994). The solid lines represent the minor (P.A. = 32°) and the major (P.A. = 122°) axes of the core. The dashed line gives approximately the orientation and extension of the outflow detected by GEVWH (P.A. $\sim 80^\circ$). The central bright source is likely associated with the source powering the molecular outflow.

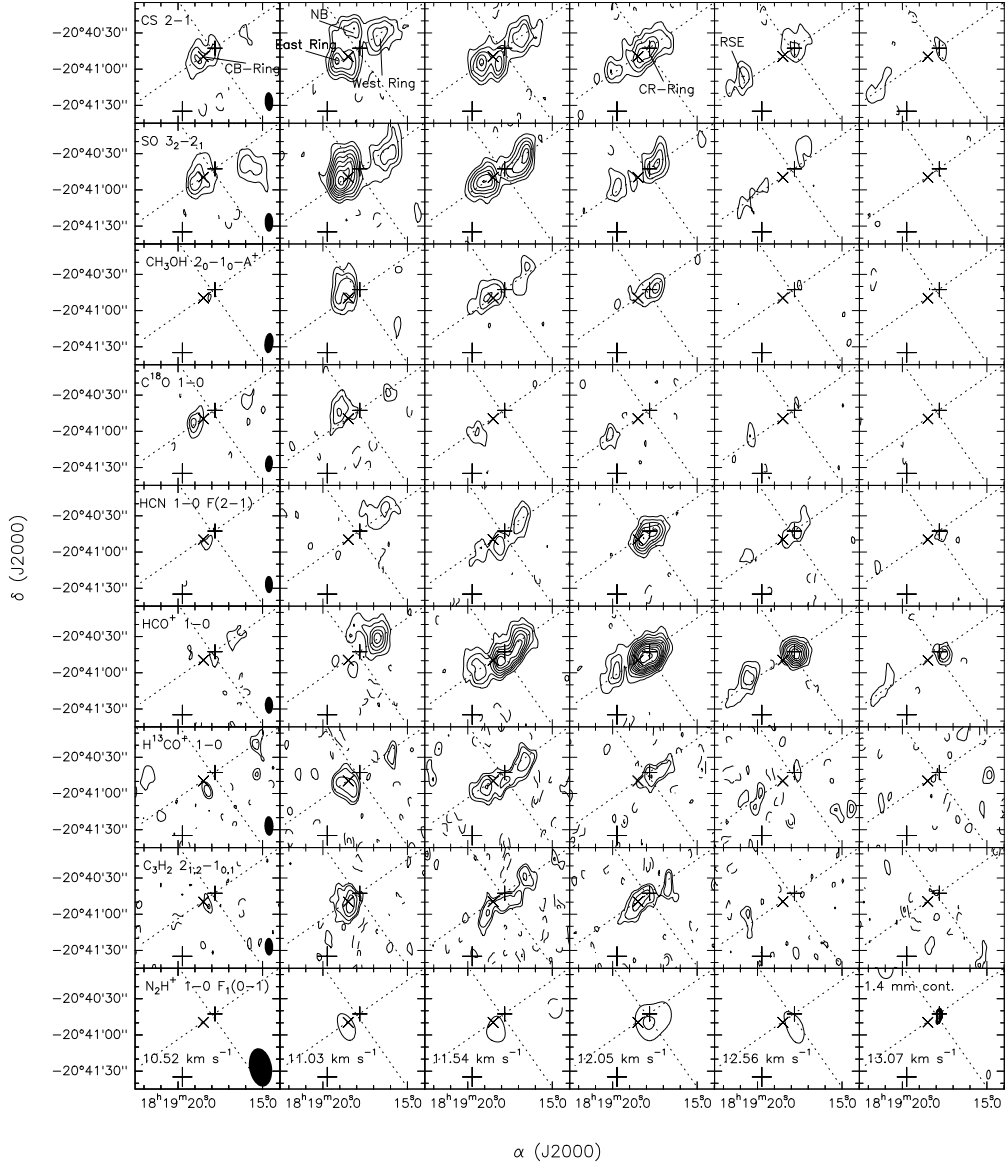


Fig. 2.— Channel velocity maps of the species shown in Fig. 1 over the 10.5 km s^{-1} to 13.0 km s^{-1} velocity range, with a velocity resolution of $\sim 0.5 \text{ km s}^{-1}$. The level contours are $-3, 3, 5, 7, 9, 11, 13, 15, 18,$ and 21 times the rms noise level for each species. For H^{13}CO^+ and C_3H_2 the contours -2 and 2 times rms the noise are also shown. The labels shown in the first row indicate the parts of the ring-like morphology (see § 3), as well as other structures. The thick solid contour shown in the bottom right panel represents 2 times the rms of the 1.4 mm continuum emission. The beam for each species (filled ellipse) is shown in the bottom right corner of the panels of the first column. The beam of the 1.4 mm continuum emission (open ellipse) is shown in the bottom right corner of the bottom right panel. The symbols are the same as in Fig. 1.

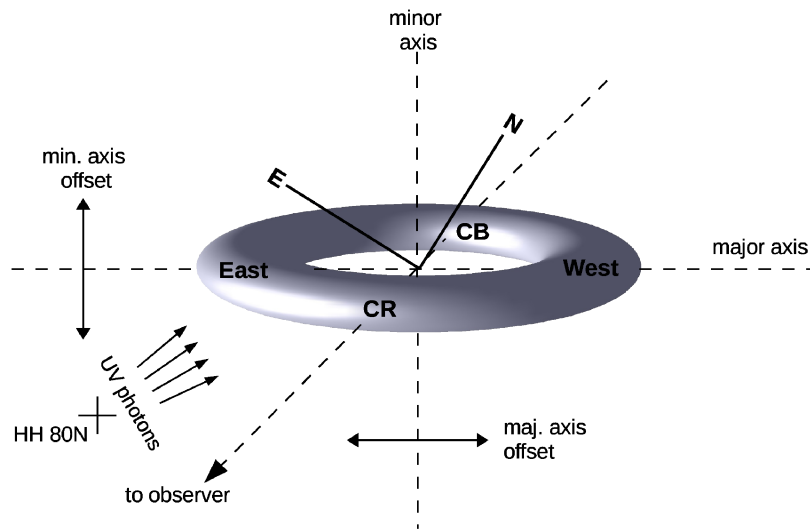


Fig. 3.— Sketch of the of the model geometry used in the analysis of the PV plots, including a schematic representation of the HH 80N scenario that we propose in order to account for the observed chemistry in the ring components discussed in § 4.2.2. Note that this figure is not plotted to scale.

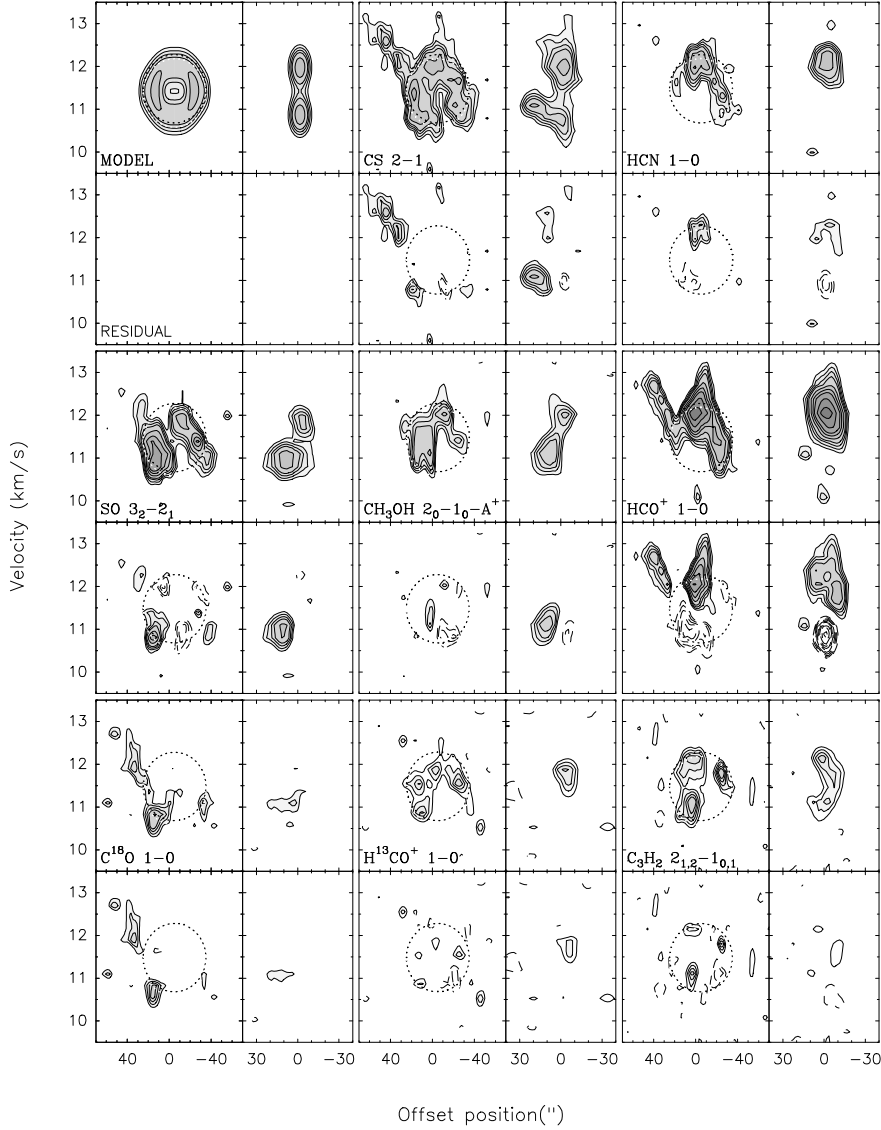


Fig. 4.— Sets of PV plots for (*from left to right and from top to bottom*): model, CS (2–1), HCN (1–0), SO (3_2-2_1), CH₃OH ($2_0-1_0-A^+$), HCO⁺ (1–0), C¹⁸O (1–0), H¹³CO⁺ (1–0) and C₃H₂ ($2_{1,2}-1_{0,1}$). For each set, the PV plots of the BIMA data are shown at the top and the residual PV plots resulting from subtracting the data and the model are shown at the bottom. The panels on the left represent the PV plots along the major axis while the panels on the right represent the PV plots along the minor axis of the core. For the set of PV plots obtained from the model, the two panels at the top show the best fit model (see text) for the major (left) and minor (right) axis of the ring-like structure seen edge-on. The positive offsets of the PV plots corresponds to South-East and to North-East directions for the major and minor axis, respectively. The contour levels are -10, -8, -6, -4, -3, 3, 4, 6, 8, 10, 12, 14, 16, and 20 times the rms noise for each species. For H¹³CO⁺ and C₃H₂ the contours -2 and 2 times the rms noise are also shown. The dashed ellipse, drawn to highlight the best fit model for the major axis, corresponds to a ring with a radius of 30″.

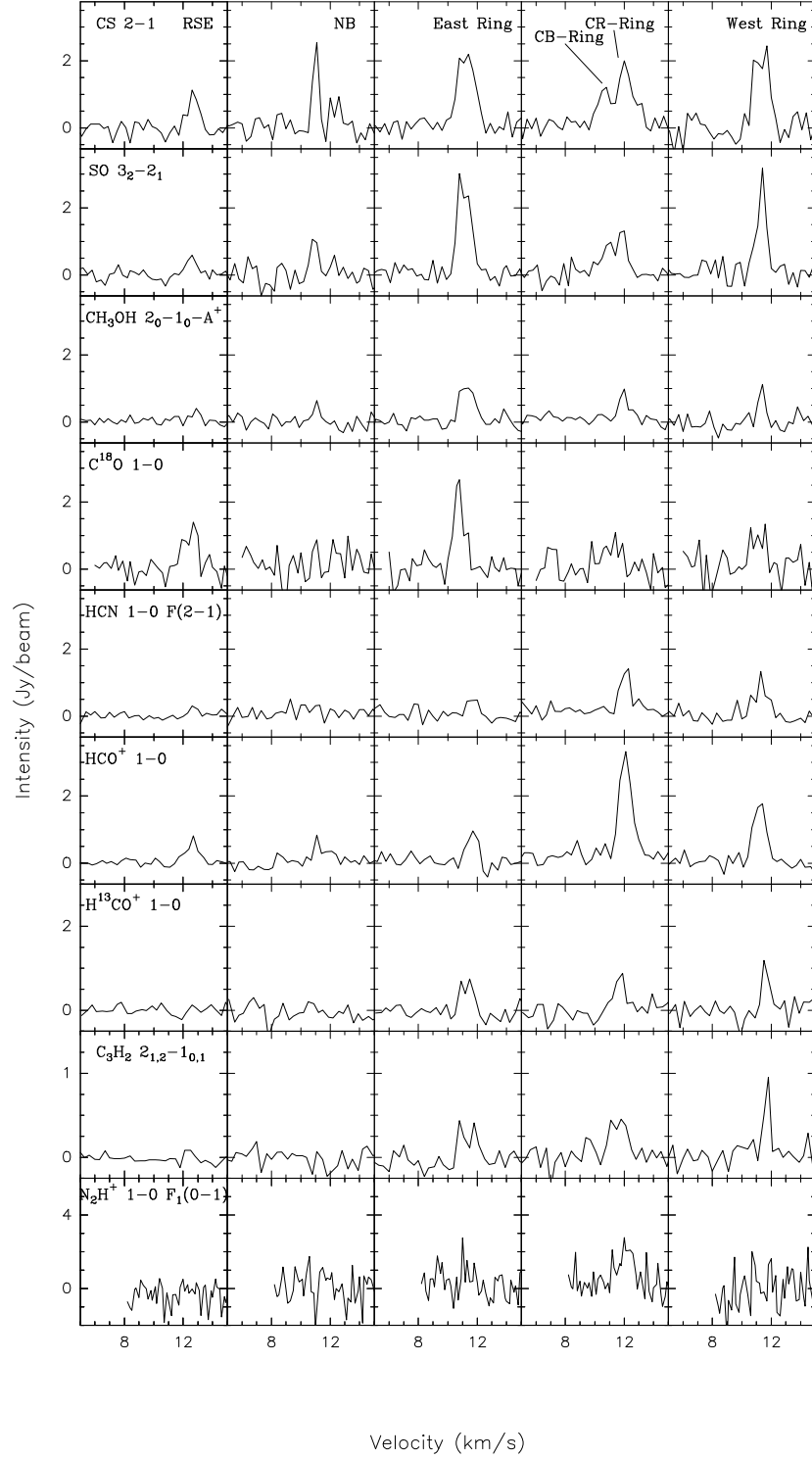


Fig. 5.— Spectra of (*from top to bottom*) CS (2–1), SO (3₂–2₁), CH₃OH (2₀–1₀)-A⁺, C¹⁸O (1–0), HCN (1–0, F(2–1)), HCO⁺ (1–0), H¹³CO⁺ (1–0), C₃H₂ (2_{1,2}–1_{0,1}), and N₂H⁺ (1–0, F₁(0–1)) towards (*from left to right*) RSE, NB, East Ring, CB and CR-Ring, and West Ring components given in Table 2. For RSE, the spectra were obtained for a box of $\sim 15'' \times 25''$.

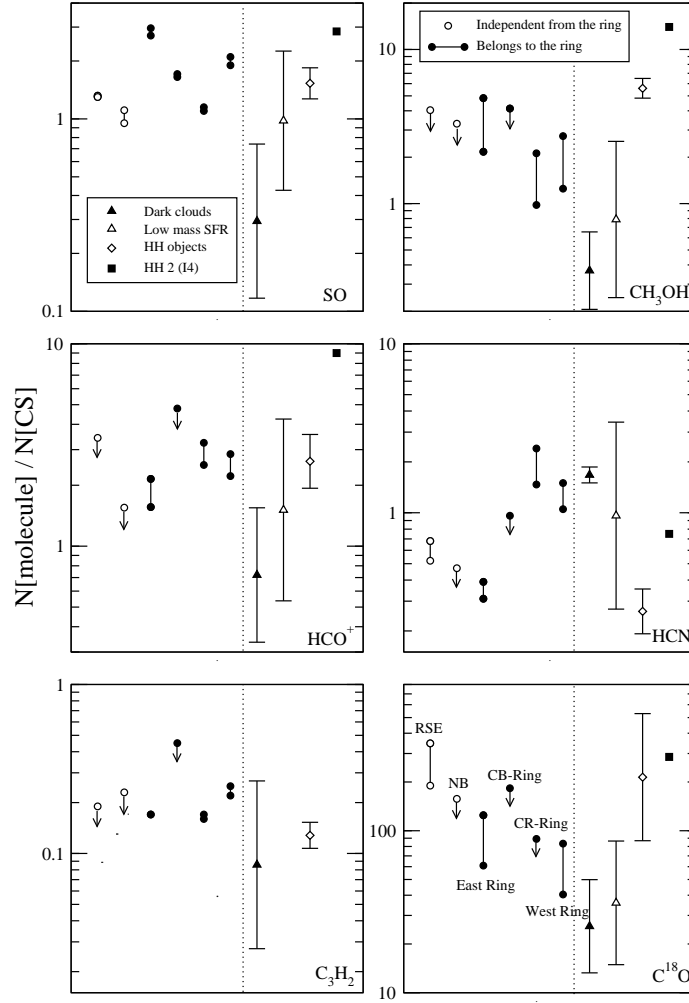


Fig. 6.— Relative molecular abundances (with respect to CS) for (*from left to right and from top to bottom*) SO, CH₃OH, HCO⁺, HCN, C₃H₂ and C¹⁸O. In each panel the circles represent the structures found for the HH 80N region: (*from left to right*) RSE, NB, East Ring, CB-Ring, CR-Ring and West Ring, and the bars between circles represent the range of relative abundances derived from the density range found in § 3.2. The rest of the symbols and the bars represent the logarithmic median and standard deviation of the relative molecular abundances for each sample (*from left to right*): dark clouds (i.e. without star formation activity), low-mass star-forming cores, regions close to HH objects, and a position close to HH 2. The sample for the quiescent dark molecular clouds is: OMC-1N (Ungerechts et al. 1997), TMC-1 (Pratap et al. 1997), L1498 and L1517B (Tafalla et al. 2006), L1544 and L1689B (Jørgensen et al. 2004), and B68 (di Francesco et al. 2002). The sample for the low mass star forming molecular clouds is: IRAS 16293 – 2422 (van Dishoeck et al. 1995), NGC 1333 IRAS 4A (Blake et al. 1995), IRAS 05338 – 0624 (McMullin et al. 1994), Serpens S68 (McMullin et al. 2000), several cores from Jørgensen et al. (2004) and Schöier et al. (2002) and CH₃OH data (Maret et al. 2005). The sample of the regions close to HH objects is: HH 2 (Girart et al. 2005), HH 1, several positions towards HH 7-11, and HH 34 (Viti et al. 2006). The HH 2 data were taken in the SO₂ clump (see Girart et al. (2005)).

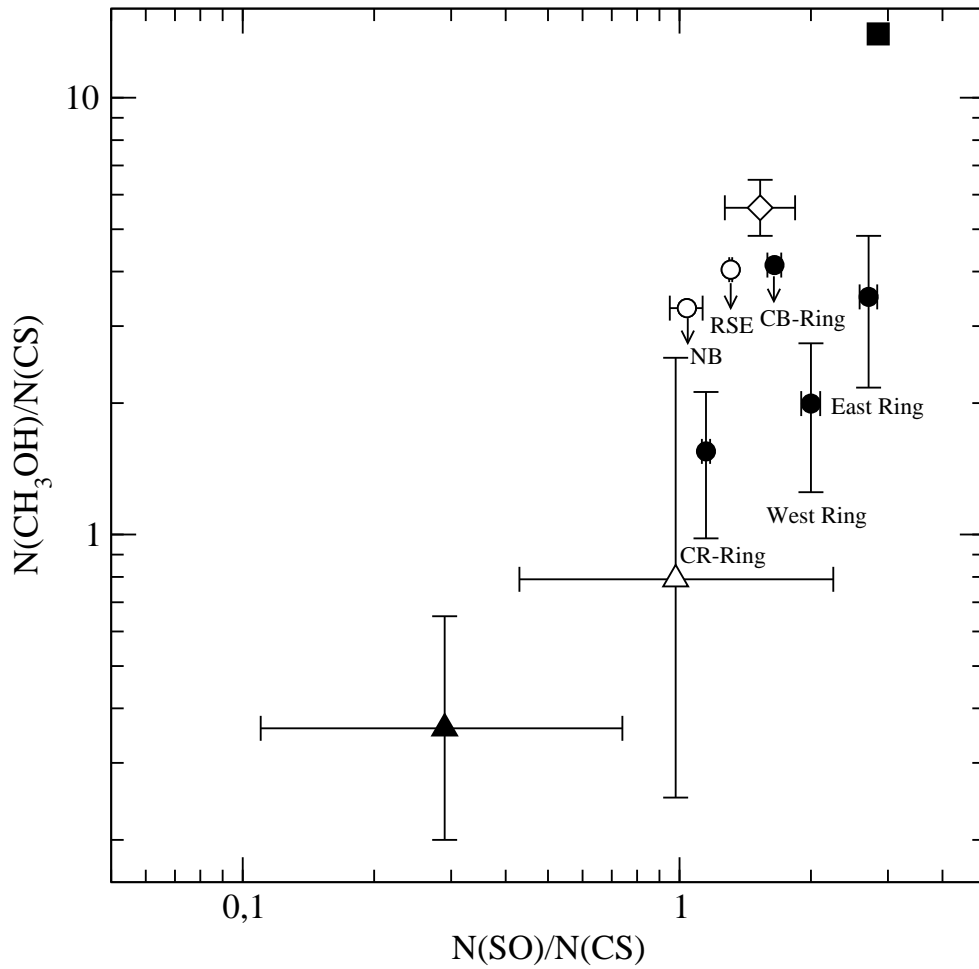


Fig. 7.— CH_3OH vs. SO relative molecular abundances (with respect to CS). The circles represent the structures found for the HH 80N region and the bars associated with the circles represent the range of relative abundances for the density range found in § 3.2. The rest of the symbols and bars are the same as in Fig. 6.